Temperature and EUV Intensity in a Coronal Prominence Cavity and Streamer

T.A. Kucera[1], S.E. Gibson[2], D. J. Schmit[3,2], E. Landi[4], D. Tripathi[5]

ABSTRACT

We analyze the temperature and EUV line emission of a coronal cavity and surrounding streamer in terms of a morphological forward model. We use a series of iron line ratios observed with the *Hinode* Extreme-ultraviolet Imaging Spectrograph (EIS) on 2007 Aug. 9 to constrain temperature as a function of altitude in a morphological forward model of the streamer and cavity. We also compare model prediction of the EIS EUV line intensities and polarized brightness (pB) data from the Mauna Loa Solar Observatory (MLSO) MK4. This work builds on earlier analysis using the same model to determine geometry of and density in the same cavity and streamer. The fit to the data with altitude dependent temperature profiles indicates that both the streamer and cavity have temperatures in the range 1.4-1.7 MK. However, the cavity exhibits substantial substructure such that the altitude dependent temperature profile is not sufficient to completely model conditions in the cavity. Coronal prominence cavities are structured by magnetism so clues to this structure are to be found in their plasma properties. These temperature substructures are likely related to structures in the cavity magnetic field. Furthermore, we find that the model overestimates the line intensities by a factor of 4-10, while overestimating pB data by no more than a factor of 1.4. One possible explanation for this is that there may be a significant amount of material at temperatures outside of the range $\log T(\mathrm{K}) \approx 5.8 - 6.7$ in both the cavity and the streamer.

Subject headings: Sun: corona, Sun: filaments, prominences

[1]NASA/GSFC, Code 671, Greenbelt, MD 20771

[2]HAO/NCAR

[3]University of Colorado, Boulder

[4]University of Michigan

[5]Inter-University Centre for Astronomy and Astrophysics

1. Introduction

Coronal cavities are the coronal manifestations of filament channels. They can be seen in cross section at the solar limb above magnetic neutral lines and below brighter coronal streamers. They surround solar prominences and in some models these features share a joint magnetic field. They are observed to erupt, forming the dark cavity in the classical three part coronal mass ejection (CME) shape of bright front, dark cavity, and bright prominence core (Gibson et al. 2006). Understanding the physical characteristic of cavities, including density and temperature as well as flow patterns and magnetic field should provide valuable clues to long standing questions concerning the triggers to CME eruption and the processes involved in the formation and maintenance of prominences.

It has been established that cavities are, as the name implies, less dense than the surrounding streamers. Cavity densities are most unambiguously determined from white-light observations, which are temperature-independent, and these indicate a lower limit of approximately half the density of a surrounding streamer at the same height (Fuller & Gibson 2009).

Temperature measurements have proven to be more ambiguous. Efforts have been made using white light data to infer a density scale height and associated "hydrostatic temperature" (Guhathakurta et al. 1992; Fuller et al. 2008; Fuller & Gibson 2009). These have indicated higher hydrostatic temperatures in the cavity than the streamer. However, these calculations require simplifying assumptions concerning the boundary conditions for cavity and streamer flux-tubes (Fuller et al. 2008). Measurements using coronal spectral lines do not require these assumptions and indicate that cavities and, in some studies, streamers are not hydrostatic. The Guhathakurta et al. (1992) white light observations were complemented by measurements of coronal red (6374 Å Fe X) and green (5303 Å Fe XIV) lines that indicated that the cavity was cooler then the streamer, contradicting the hydrostatic white light calculations for the same cavity. Vásquez et al. (2009) used tomographic analysis of streamers and cavities using data from the Extreme Ultraviolet Imager (EUVI) aboard the *Solar Terrestrial Relations Observatory (STEREO)* and found that the cavity temperature distribution was broader and extended to higher temperatures than did those of the surrounding streamers.

Cavities also appear to have internal substructure in temperature. Hudson et al. (1999) and Reeves et al. (2012) report soft x-ray emission has been observed surrounded by an otherwise low-emission cavity, and "hot shrouds" around prominences associated with cavities have been observed in visible and IR emission (Habbal et al. 2010). Such hot cores are often but not always present within cavities, and may have a disk-like or ring-like shape (Reeves et al. 2012). They extend to heights well above the prominence, but do not fill the cavity.

In this analysis we have used a morphological forward model to analyze a cavity and surrounding streamer observed in 2007 August. This paper is third in a series. In the first paper, Gibson et al. (2010) (Paper I) data from *STEREO*/EUVI were used to determine the morphological parameters of the model in which the cavity is modeled as a long low-density tube of varying cross section in a coronal streamer. Schmit & Gibson (2011) (Paper II) then used data from the *Hinode*/Extreme-ultraviolet Imaging Spectrograph (EIS) and the Mauna Loa Solar Observatory Mark 4 K-coronameter (MLSO/Mk4) to forward model both a density sensitive Fe XII line ratio and white light data to determine density as a function of altitude in the cavity and the streamer. They found an average density depletion of the cavity relative to the streamer of about 30%.

Here we build on these previous results by using observations of a series of iron lines observed by EIS to forward model the temperature profile in the cavity and streamer. We also compare the extreme ultraviolet (EUV) intensity values in order to determine the filling factor in the streamer and cavity.

In the following section we describe the observations and data reduction. In § 3 we discuss the forward model and the analysis of the data in terms of the model, and in § 4 we discuss the possible interpretations of our analysis and modeling of temperature and EUV line intensities. The final section summarizes our conclusions.

2. Data and Data Reduction

This cavity was observed in 2007 August as part of a campaign associated with the International Heliophysical Year (IHY). The full set of multi-instrument observations is described in Paper I. The cavity was over a polar crown prominence in the north-east. Rasters from six of the lines observed with EIS are shown in Figure 1. The basic elliptical cavity structure is most clear in the Fe X, Fe XI, and Fe XII raster images. The images produced by the hotter lines, especially Fe XV, show a more complex array of structures. We also show the Fe VIII 185.21 Å raster from EIS and, in Figure 2, He II 304 Å and Fe XII 195 Å band images from the *Solar and Heliospheric Observatory*'s Extreme-ultraviolet Imaging Telescope (*SoHO*/EIT) to show the location of the prominence.

2.1. EIS Fe line data

The EIS data used were extracted from the same raster as those used for the density sensitive line ratio analysis in Paper II. EIS (Culhane et al. 2007) is a slit spectrometer taking

data in the ranges 171-212 Å and 245-291 Å, but only selected lines are telemetered down during most observations. The EIS raster was taken from 2007 Aug. 9 14:19:20 -18:42:30 UT, with a step size of $1''$ and exposure time of 60 sec. Pixel size along the slit was also $1''$. Original images were $256 \times 256''$. The data were analyzed with the standard eis_prep routines available in SolarSoft (Young et al. 2009; Young 2011). We used the optional correction for CCD degradation over time. This correction led to a increase in intensity values of 18.5% from the uncorrected data. In order to increase signal-to-noise the data were binned by a factor of 6. Data from different lines were aligned using the EIS routines that correct for pointing shifts as a function of wavelength and then aligned with other data sets using off sets calculated for the work in Paper II.

For our temperature analysis we used a series of lines, listed in Table 1. For densities $\gtrsim 10^9$ cm^{-3} the lines are density insensitive beyond the normal n_e^2 dependence of collisionally excited lines from allowed transitions. This minimizes the dependence of their ratios on the model of density developed in Paper II.

2.1.1. EIS Scattered Light

Because cavities are relatively low intensity features we also attempted to correct the data for stray light contamination. Ugarte-Urra (2010) used data from a partial lunar eclipse of the Sun as seen by *Hinode* to estimate that the stray light component to EIS emission is a minimum of 2% of the average on-disk emission at a given wavelength. Hahn et al. (2011) used this result when analyzing data in a coronal hole, applying a stray light correction based on 2% of the on-disk values as measured from the portion of their raster that included on-disk data. They checked this method by analyzing on and off disk emission from a He II, Si X blend at 256.3 Å and Si X at 261.0 Å, and found that the 2% value seemed reasonable.

We employed a similar method, subtracting off a value of 2% of the average disk emission in each line. This is probably larger than the factor used by Hahn et al. because they were using coronal hole data while we were observing adjacent to the quiet Sun. We find that the importance of this correction is highly dependent on the temperature of formation of the line due to the temperature dependent contrast between disk and off limb emission. For the Fe X emission, which falls off rapidly with altitude, the correction is about 10% at an altitude of 1.1R$_\odot$ and 35% at an altitude of 1.6R$_\odot$, whereas for the Fe XV emission the correction never exceeds 2%.
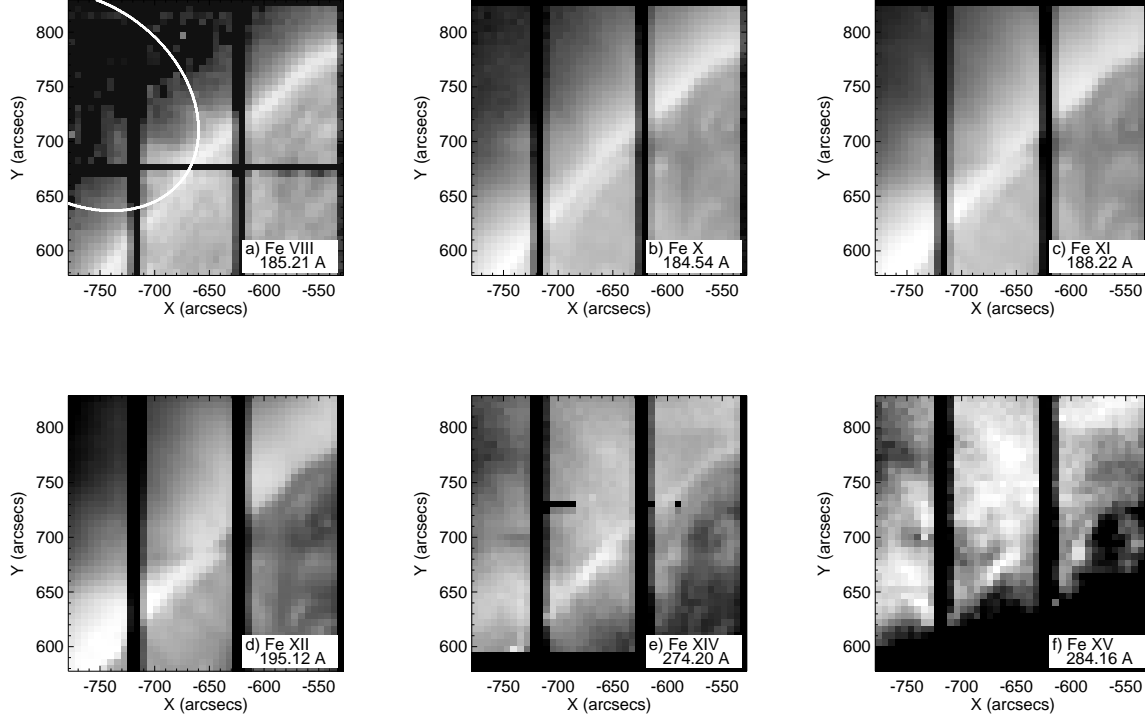
Fig. 1.— EIS raster images taken 2007 Aug. 9 from from 14:19:20 -18:42:30 UT. Intensities are in log scale. The images have been binned to a resolution of 6″. The Fe VIII image (a) is included to show in location of the prominence in emission at transition region temperatures ($\approx 500,000$ K). It is also overlaid with a curve showing the border of the model cavity in the plane of the sky. Other data shown (b-g) are used in our temperature analysis.

Ion	λ	Transition	L1	L2
Fe X	184.54	$3s^2\ 3p^5\ ^2P_{3/2}$ - $3s^2\ 3p^4\ (^1D)\ 3d\ ^2S_{1/2}$	1	27
Fe XI	188.23	$3s^2\ 3p^4\ ^3P_2$ - $3s^2\ 3p^3\ (^2D)\ 3d\ ^3P_2$	1	38
Fe XII	195.12	$3s^2\ 3p^3\ ^4S_{3/2}$ - $3s^2\ 3p^2\ (^3P)\ 3d\ ^4P_{5/2}$	1	27
Fe XIV	274.20	$3s^2\ 3p\ ^2P_{1/2}$ - $3s\ 3p^2\ ^2S_{1/2}$	1	8
Fe XV	284.16	$3s^2\ ^1S_0$ - $3s\ 3p\ ^1P_1$	1	5

Table 1: Spectral Lines Used in Temperature Analysis

2.2.   MLSO Mk4

In this paper we also present polarized brightness (pB) data taken by the MLSO/Mk4 Coronagraph Polarimeter (Elmore et al. 2003). These data and their analysis are described in Papers I and II. The Mk4 data for this streamer and cavity extend from 1.17-1.50 R$_\odot$. This lower limit of this range range is slightly higher than that of the EIS data used in our analysis, which extend up to 1.163 R$_\odot$ in the cavity and 1.144 R$_\odot$ in the streamer (see §3.2).

3.   Analysis

3.1.   Model

In order to more carefully analyze possible line-of-sight effects (for instance, streamer material in the foreground and background of the cavity), we utilize a morphological cavity model. The cavity is modeled as a tunnel like structure in an elongated streamer with elliptical cross-section and a Gaussian variation in height along the tunnel length.

In Paper I Gibson et al. (2010) determined the dimensions of the cavity by fitting the shape of the cavity in limb EUV observations of a cavity over the course of several days using different points of view provided by the two *STEREO* spacecraft. Paper II also presents slight adjustments to the streamer and cavity geometry, and we include those changes here.

In Paper II Schmit & Gibson (2011) forward fit a density-sensitive Fe XII line ratio and MLSO/Mk4 polarized brightness (pB) data using separate density profiles for the cavity and streamer. Here we use slightly different density values based on the EIS ratio alone. These best-fit densities are:

$$n_{e}\mathrm{str} = (3.05r_{piv}^{-18} + 2.56r_{piv}^{-11.6} + 1.18r_{piv}^{-3.94}) \times 10^8 \mathrm{cm}^{-3} \tag{1}$$

$$n_{e}\mathrm{cav} = (3.0r^{-23.1} + 1.63r^{-16.3} + 1.53r^{-5.64}) \times 10^8 \mathrm{cm}^{-3} \tag{2}$$

where r is the altitude and r_{piv} is the altitude in the coordinate frame of the non-radial streamer, both in units of R$_\odot$. The streamer profile in Equation 1 is valid at the central axis of the streamer, and then merges into a spherically symmetric background with a Gaussian falloff in the manner described in Gibson et al. (2003). We use this new expression for density to better evaluate the possibility of a filling factor (see § 4.2). The cavity density profile is not significantly different from the range of fits discussed in Paper II, but the streamer profile becomes about 20% higher than the earlier best fit for altitudes $\gtrsim$ 1.2 R$_\odot$. In the altitude range of 1.05 to 1.20 R$_\odot$ model streamer densities range from 4.0×10^8 (at the low

altitude limit) to 1.2×10^8 cm^{-3}, and cavity densities range from 2.9×10^8 to 0.7×10^8 cm^{-3}, values well within the range at which the lines we use are density insensitive.

For this work we introduce a temperature variation in terms similar to the density variation, but with the temperature going to zero at the photosphere. This is physically plausible and results in better fits with fewer parameters than having the zero point at $r = 0$.

$$T_{\text{str}} = S_0(r_{piv} - 1)^{S_1} + S_2(r_{piv} - 1)^{S_3} + S_4(r_{piv} - 1)^{S_5} MK \tag{3}$$

$$T_{\text{cav}} = C_0(r - 1)^{C_1} + C_2(r - 1)^{C_3} + C_4(r - 1)^{C_5} MK. \tag{4}$$

As for the density, the streamer profile in Equation 3 is valid at the central axis of the streamer, and then merges into the background with a Gaussian falloff; the cavity temperature is entirely determined by Equation 4.

In order to model the response of the EIS lines we assumed a collisional plasma in which the line intensity is an integral along the line of sight,

$$I = \int_{\text{los}} n_e^2 G(n_e, T) dl, \tag{5}$$

where n_e is the electron density, and $G(n_e, T)$ is the contribution function for each spectral line. We do not expect a significant radiative scattering component for these lines at the altitudes we are considering in this work. We have selected lines for which the contribution function has very little density dependence, so that the remaining n_e^2 dependence is divided out and the line ratios are essentially independent of density.

The contribution function values were calculated using the Chianti data base version 7.0 (Dere et al. 1997; Landi et al. 2011). We used the coronal abundances of Feldman et al. (1992), the Chianti ionization equilibrium calculations (Dere et al. 2009), and assumed a hydrogen to electron ratio of 0.83.

All lines used for the temperature analysis were deemed appropriate for emission measure analysis by Warren & Brooks (2009) except for the Fe XV 284.16 Å line. There were no indications of problems with that line, but there are no other lines in the EIS range with which it could be checked. We considered possible lines that might be blended with our main observational lines. We found that including the blend of the Si VII 274.18 Å line with the Fe XIV 274.20 Å line and Ar XI 184.52 Å with Fe X 184.54 Å led to detectable variations in our model intensities, and so included them in the model calculations. However, these variations were small compared both to the uncertainties in the data and the model, so the inclusion of these lines does not affect our ultimate conclusions.

The pB is dependent only on electron density and altitude, with no temperature component,

$$pB = \int_{\text{los}} n_e C(r) dl, \tag{6}$$

where $C(r)$ is a Thompson scattering function (Billings 1966; Fuller et al. 2008).

3.2. Temperature Ratio Analysis

In Figure 4 we show the regions used in the temperature analysis. These are very similar to those used in Paper II, but with a larger area around the prominence removed. Although it would be interesting to consider conditions in the prominence, the possible presence of Lyman absorption by the prominence would make the analysis difficult. The data for the density fit came from the larger area used in Paper II, but this affects the model density values by less than 10%. The points are divided into "cavity" and "streamer" categories, although each individual point may have both cavity and streamer contributions along the line of sight, as shown in Figure 4c. The plane of sky altitude range for the points used is 1.050- 1.163 $R_\odot$ for the cavity and 1.045-1.144 $R_\odot$ for the streamer.

To analyze temperatures we fit ratios of the lines listed in Table 1. Each line was divided by the line with the next hottest temperature of formation. An downhill simplex "amoeba" method (Nelder & Mead 1965) was used to determine the best fits. Maps of the ratio data are show in Figure 5.

In addition to the temperature profile parameters we found it necessary to introduce parameters designed to correct for uncertainties in atomic physics. It was clear from our initial fits to the data that there were some systematic difficulties in fitting the different ratios. These were consistent with uncertainties in the atomic data often considered to be as high as 20%, as discussed in § 3.4. To counteract the effects of these uncertainties on our results we introduced variable parameters corresponding to a multiplicative factor for each of the lines. We found that a factor of 0.85-0.9 applied to the model Fe XI 188.2 Å intensities dramatically improved the fits to the temperature ratios, while smaller corrections were indicated for the other lines.

Our best fit parameters are presented in Table 2. Figure 6 shows the corresponding data and model values as a function of altitude for each of the line ratios. In Figure 7 we show the temperature as a function of altitude.

It is difficult to determine the confidence level for these fits. Using only the Poisson and dark current uncertainties to the data points the χ^2_ν values are quite high (> 3). We think
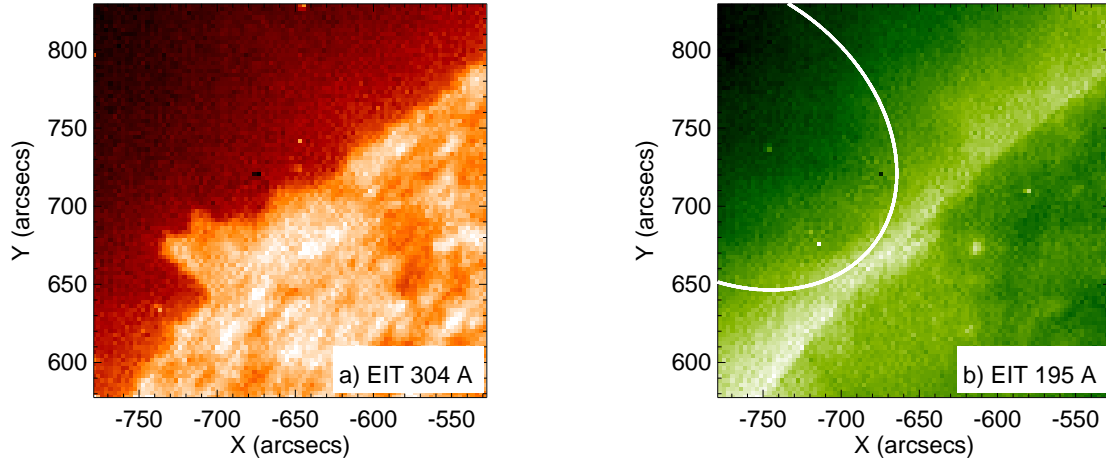
Fig. 2.— Images from *SOHO*/EIT on 2007 Aug. 9 in a) the 304 Å band at 18:35:19 UT and b) the 195 Å band at 13:12:32 UT for comparison with the EIS images in Fig. 1. Overlaid on the 195 Å band image is the boundary of the model cavity in the plane of the sky as determined in Paper I.

Streamer Temp. Param.:	S_0:1.302	S_1: 0.172,	S_2:-0.389	S_3:0.751	S_4:0.967	S_5:0.120
Cavity Temp. Param.:	C_0:1.218	C_1:-0.281	C_2: -0.124	C_3:-0.818	C_4:0.783	C_5:1.105
Multiplicative factors for spectral lines:	Fe X:0.96	Fe XI:0.85	Fe XII:1.00	Fe XIV:1.04	Fe XV:1.00	

Table 2: Temperature Ratio Fit Parameters.
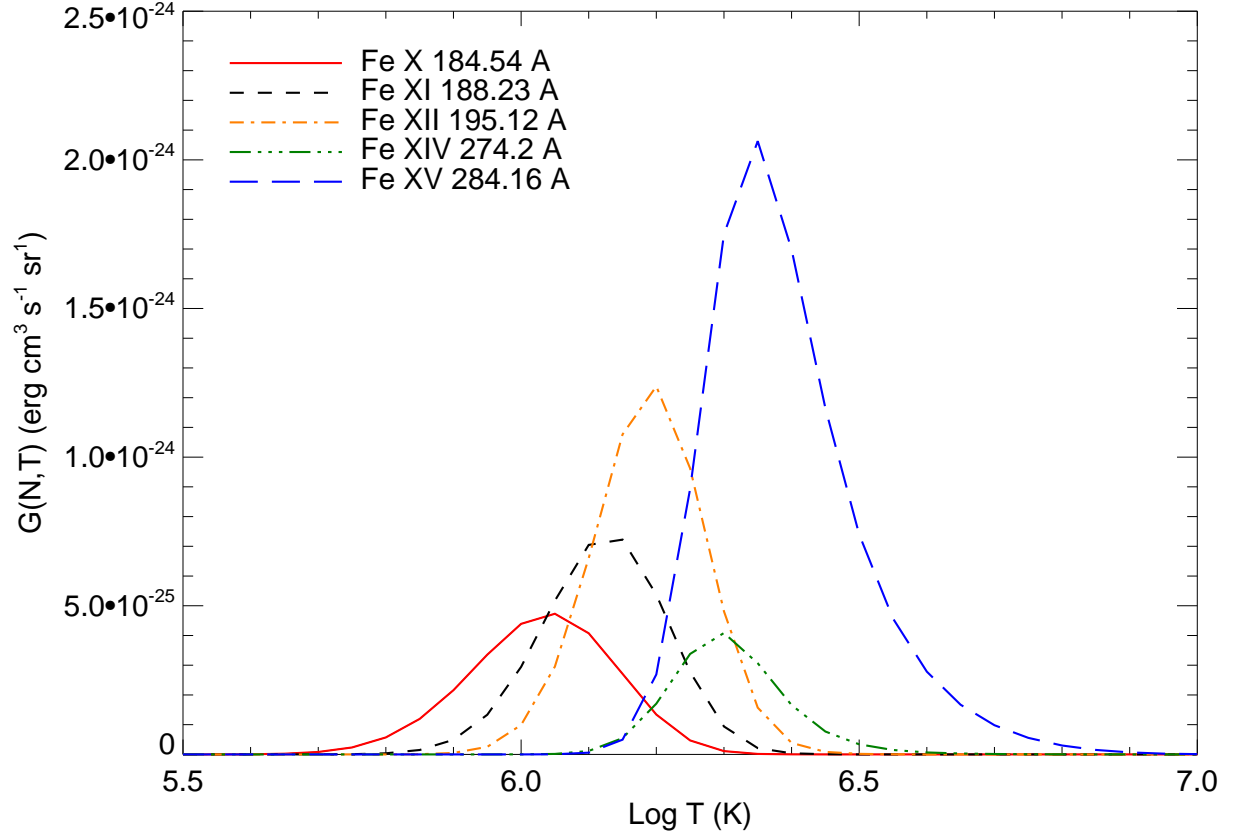
Fig. 3.— Contribution functions for the lines used in this investigation. These values include elemental abundances and the n_H/n_e ratio.
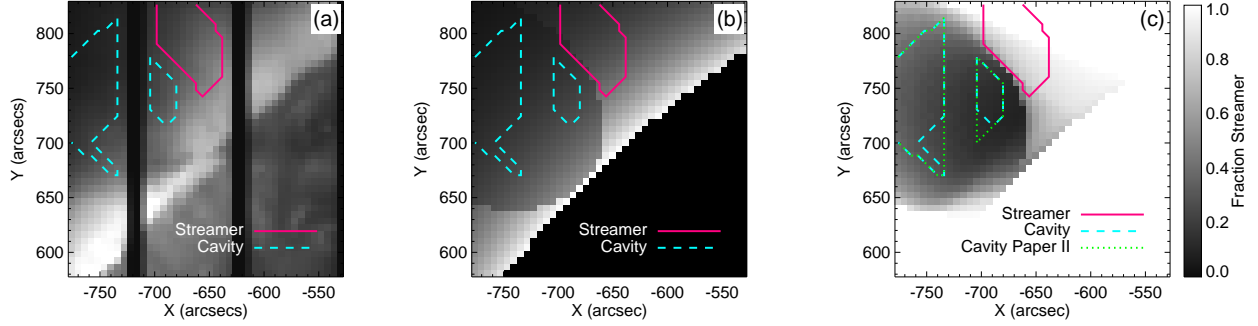
Fig. 4.— Location of the points designated "cavity" and "streamer" in Figs. 6. These are superimposed on a) the EIS Fe XII data and b) the density in the plane of the sky from the morphological model (center). These points are not necessarily pure cavity or streamer along the line of sight, but tend to be dominated by emission from one region or the other. Panel (c) shows the fraction of emission from the streamer as opposed to the cavity at each pixel for a typical model fit. Panel (c) also shows the region used for the density modeling.
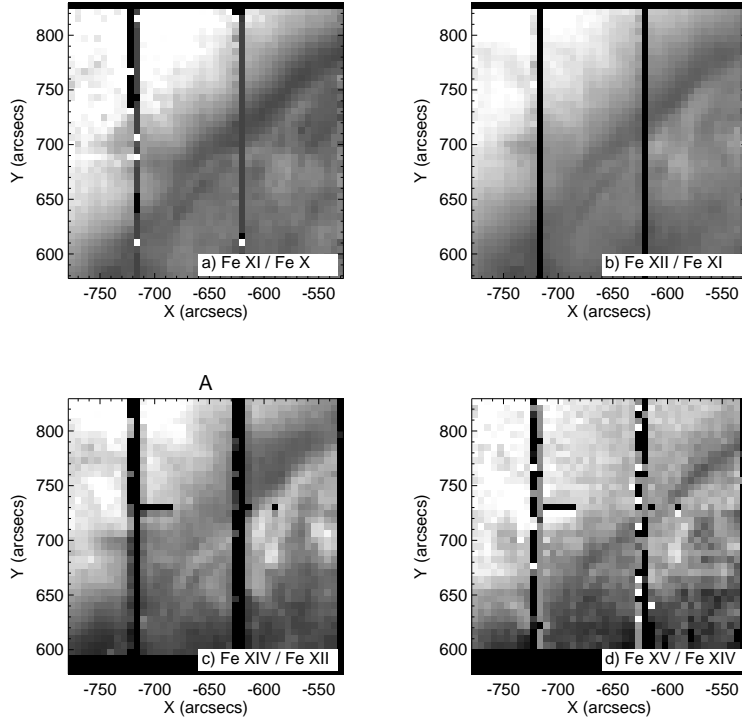
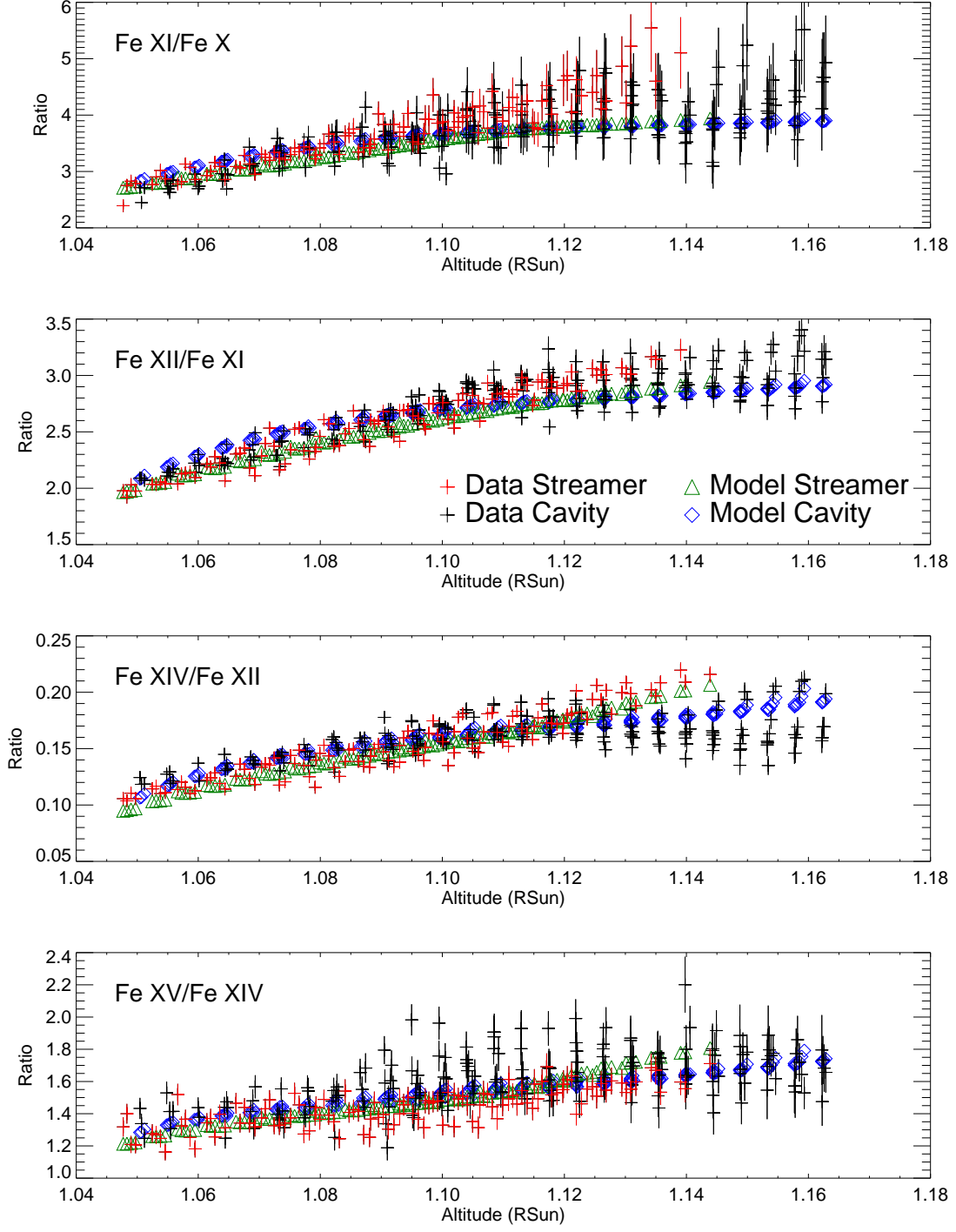Fig. 5.— Maps of the spectral line ratios

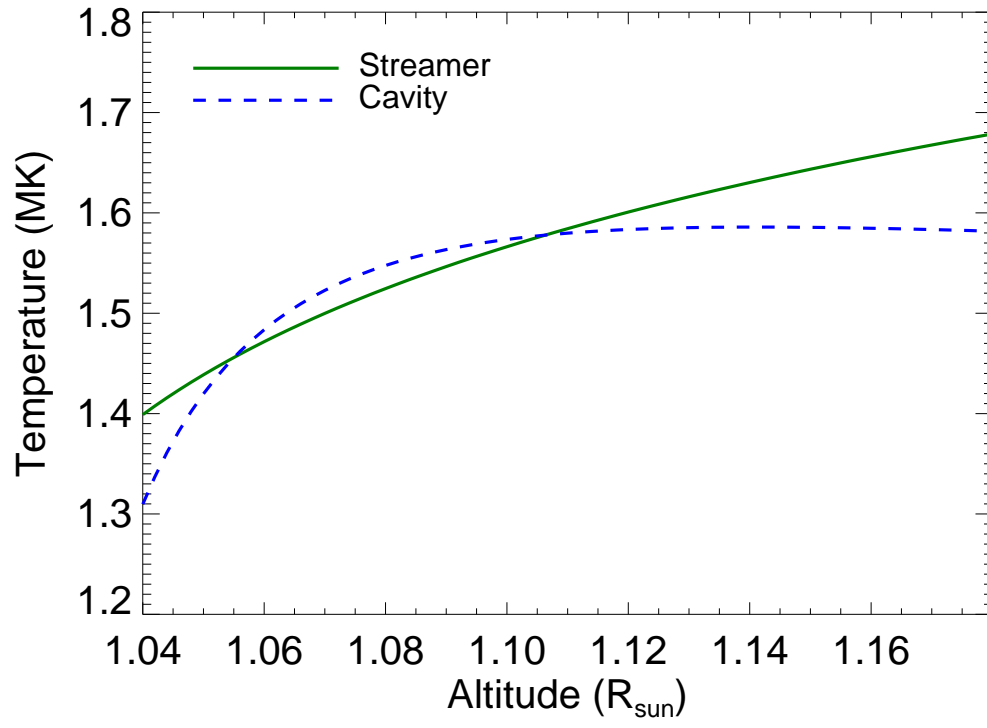Fig. 6.— Line ratios vs. altitude for data used for fit and model.

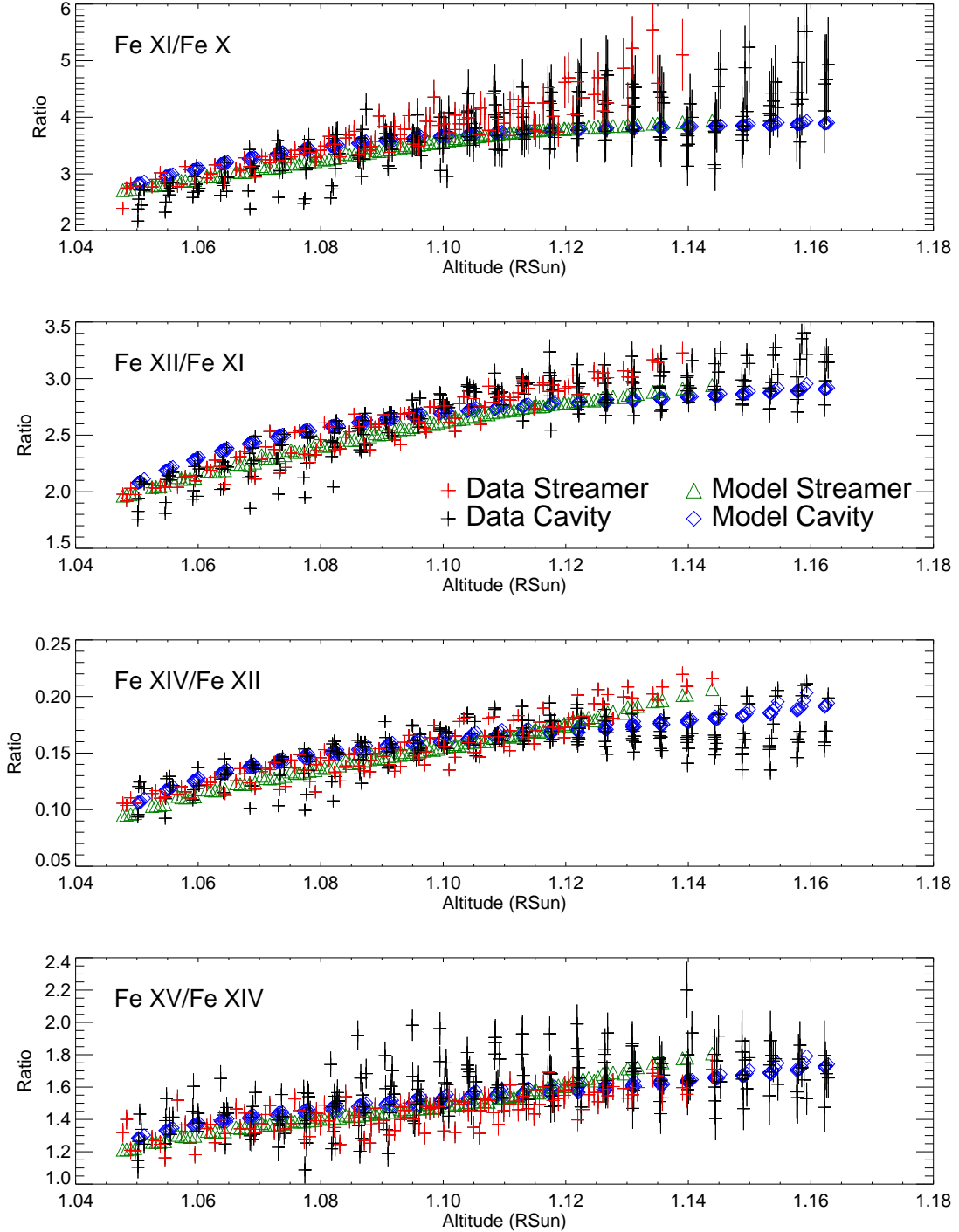Fig. 7.— Temperature profiles corresponding to the fit parameters in Table 2

Fig. 8.— Line ratios vs. altitude for data, including data near the prominence that was not used in the fit, and model. The prominence data were taken out for the fitting in case the area exhibited Lyman absorption that might harm the results. Here we include it to show that the cavity substructure variations extend through a wide range of altitudes.

there are two main contributing factors to this. One is that there are a number of significant systematic uncertainties that are hard to quantify. These are discussed in more depth in § 3.4. The other reason is that, particularly in the cavity, there are true variations in the line ratio data that are not adequately modeled using simple radial temperature profiles. These variations can be seen in both Figures 5 and 6. However, despite these factors, the model seems to match the general variations with altitude fairly well, although there is a tendency for the model to underestimate the Fe XI/Fe X and Fe XII/Fe XI ratios in the streamer for altitudes $\gtrsim 1.10$ R$_\odot$.

3.3. Intensity analysis

We also compared the model and data intensity, shown in Figure 9. We found that the ratio of the EIS line intensity data to the model is about 0.15 with a slight increase with altitude. This is significantly different from the pB data-to-model ratio shown in Figure 10. We discuss possible explanations for this in § 3.4 and 4.2.

3.4. Uncertainties

As mentioned above, there are a number of uncertainties that are hard to quantify well enough to include in an analysis in the goodness of our fits. All of these have the potential to affect the intensity calculations, but uncertainties in the atomic physics of the spectral lines and stray light are the ones likely to affect the line ratios.

In general, uncertainties in atomic physics are in the 20% range (e.g., Del Zanna 2010). We attempt to correct for these uncertainties to some extent with our line correction factor (see Table 2). A single correction for each line seems reasonable because of the relatively constrained range of temperatures and densities used in the model, but may not completely take care of any problems. Based on pre-flight calibrations (Lang et al. 2006), the uncertainties in the absolute radiometric calibration of EIS are 22%.

For the density values there are possible uncertainties associated with both the fitting procedure and the atomic physics. In Paper II the estimated fit uncertainties (at a 90% confidence level) of the cavity density are about 30% (at 1.17 R$_\odot$) or better for lower altitudes. The streamer density uncertainties are thought to be 15% or better. More important are probably the uncertainties associated with the Fe XII 186.880/195.119 Å line ratio used to calculate the density. Warren & Brooks (2009) compared the results of various density diagnostics in the quiet corona, finding a variation in density of a factor of 2. The Fe XII
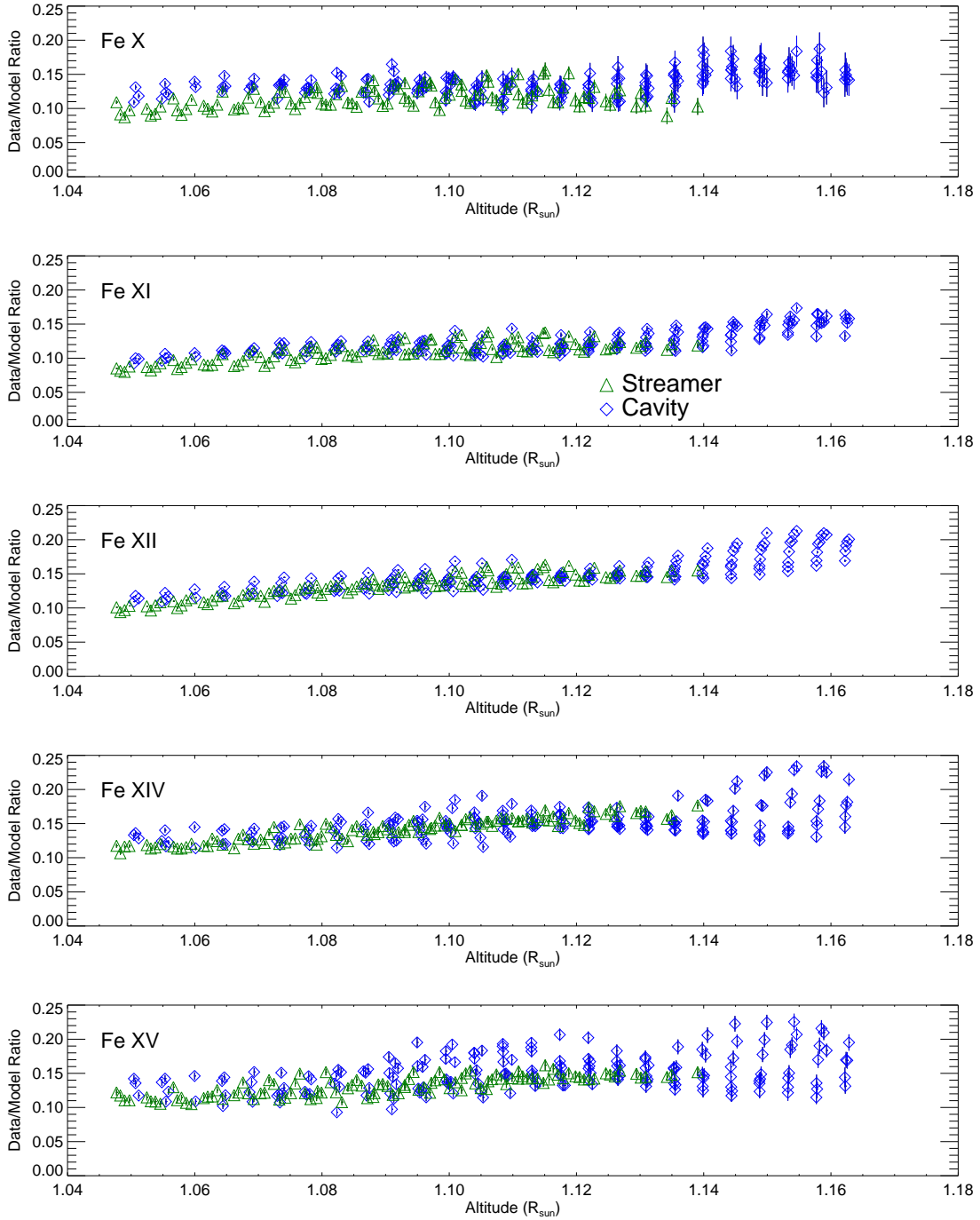
Fig. 9.— The ratio of the data and the model EUV line intensities. Error bars shown are 1σ uncertainties based on the Poisson and dark current uncertainties of the EUV line intensity data. Not included are uncertainties related to EIS radiometric calibration, abundances, density, or scattered light.
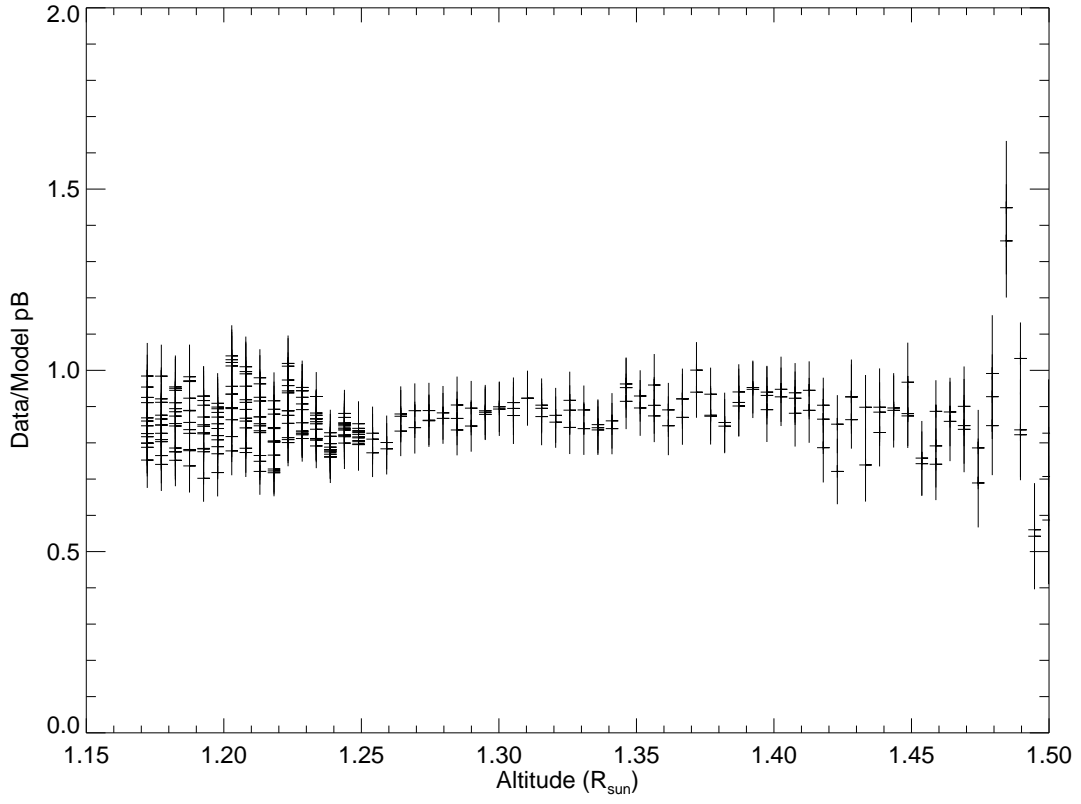
Fig. 10.— The ratio of the MLSO/Mk4 data and the model pB. Error bars shown incorporate uncertainties in calibration optics values, sky transmission, and pointing as described in Elmore et al. (2003).

186.880/195.119 Å ratio used in our density modeling was a factor of 1.12 higher than the average value considered most reliable. Young et al. (2009) compared densities calculated using the Fe XII 186.880/195.119 Å ratio with different Fe XIII based ratios and found that the Fe XII ratio averaged about 2.7 dex higher than the Fe XIII ratios. For our densities this would be a factor of about 1.8. Because the EUV intensities depend on the square of the density (Fig. 5), such an overestimation of the density could lead to an overestimation of a factor of about 3 in the EUV intensities.

As discussed in § 3, we have applied a stray light correction to these data. This is a rough estimate, however, so there is some amount of residual uncertainty related to stray light. To estimate how this may affect the data we can compare the stray light corrected data to uncorrected data. The correction reduces the quality of the fit to the Fe XI/Fe X ratio at higher altitudes but, it does not affect the model temperature values greatly. In part this is because it is divided out somewhat in the line ratios so that the change in the Fe XI/Fe X ratio is less than 20% at $1.16R_\odot$. Also, that ratio, which is most greatly affected by the stray light, is the one that has the greatest count-based uncertainties. An introduction of increased uncertainties proportional to the stray light correction also does not greatly affect the fits.

Another factor that should be considered are uncertainties in abundance values. In this investigation we are using abundance values derived from sources in the quiet portions of the lower corona (Feldman et al. 1992; Feldman 1992). For a low first ionization potential (FIP) element like iron such coronal abundances are thought to be approximately four times larger than abundances in the photosphere (Feldman & Widing 2002). However, Spicer et al. (1998) present evidence that the abundances of low FIP elements in prominences may be photospheric or midway between coronal and photospheric abundances. If this were the case and the prominence plasma has condensed out of the hotter plasma of the cavity, then such abundances might also apply to the cavity. Observations of streamers at altitudes similar to those we observe here usually indicate FIP effects of about 4, as are used in this study (Feldman et al. 1998, 2009), although there are some results from quiet sun plasmas that suggest lower abundances of low FIP elements. (Parenti et al. 2000; Warren & Brooks 2009). If this were the case it would not affect our temperature ratio results, but could effect the line intensities.

4. Discussion

4.1. Streamer and Cavity Temperature

The fit to the general radial temperature trends indicates that the temperature in both the cavity and streamer ranges from about 1.4 MK at 1.04 $R_\odot$ to about 1.6 MK in the range 1.14-1.16 $R_\odot$ (Fig. 7). There is some difference in the shape of the model profile, but it is difficult to say if it is significant. The cavity temperature, however, does seem to level off around 1.10 $R_\odot$, while the streamer temperature continues to rise.

Numerous studies (e.g., Gibson et al. 1999; Feldman et al. 1999; Alexander 1999; Parenti et al. 2000, 2003) have analyzed temperatures of streamers at altitudes overlapping with those we consider. Temperature values are generally within 25% of those we measure here. Analysis of the same streamer can yield different results. For instance, Gibson et al. (1999) and Alexander (1999) analyzed the same streamer using an EUV line ratio and soft-x-rays respectively and found that the temperatures derived from the X-ray data were 10-20% higher than the EUV derived ones. Parenti et al. (2003) analyzed the same streamer with different line ratios and found differences in the resulting temperatures of 10-30%. Generally, although not always (see Feldman et al. 1999), an increase with altitude is seen, usually with a somewhat more shallow slope ($\approx$ 1) than we see in our streamer temperature profile where the slope is close to 2.

In addition to this radial increase, however, the cavity exhibits substructure variations. This is noticeable in the spread of values in the radial plots (Figs. 6 and 8) and in structures apparent in the ratio images (Fig. 5). In particular, the Fe XIV to Fe XII ratio shows two separate features at altitudes $\geq$ 1.14 $R_\odot$. In Fig. 6 it appears that the substructure increases with altitude, but this is partly because variations at lower altitudes that appeared to be connected to the prominence were removed because of possible contamination of the EUV intensities by Lyman absorption. Fig. 8 is identical with Fig. 6 except that the emission in the extended prominence (see Fig. 4c) have been added to make this point.

There have been earlier observations of temperature substructures within cavities. Hudson et al. (1999) and Reeves et al. (2012) reported seeing hot features in coronal cavities observed in soft X-rays with *Yohkoh*/Soft X-ray Telescope (SXT)and *Hinode*/X-ray Telescope (XRT) respectively. In particular, Reeves et al. applied a version of the same forward model used in this analysis to a different cavity observed in 2008 July. It included no radial variation in temperature, but incorporated a source inside the cavity with enhanced density and temperature. Both direct analysis of the XRT data and forward modeling show that the data are consistent with a general cavity temperature of 1.4 MK plus a hot source with temperatures between 1.7-2.0 MK. The source showed substantial variation on scales of hours

or less.

Vásquez et al. (2009) used a tomographic technique applied to *STEREO*/EUVI images in the 171, 195, and 284 Å bands to analyze two steamers with cavities. They found a broader and hotter temperature distributions in the cavities than the streamers. We do not see any evidence for hotter plasma in the cavity than the streamer, although a broader temperature distribution might be consistent with cavity substructures that we do see in this study.

In our case we may have signs of a similar cavity substructure but without the localized high temperature source that would make it more obvious.

It is likely that such variations reveal magnetic structures in the cavity. In simulations performed by Luna Bennasar et al. (2012) the foot points of particular field lines in a sheared arcade model were subject to heating and the resulting motion and temperature variations along the field lines were calculated in terms of the thermal-nonequilibrium model (Karpen & Antiochos 2008, and references therein). The resulting end-on images, as in the case of a cavity on the limb, exhibit complex features in various temperatures following the twisted magnetic field lines in the cavity.

4.2. Line Intensities

We find that, for all the lines we study, the model overestimates the line intensities by a factor between 4-10 that decreases with altitude. This factor is substantially greater than the uncertainties associated with calibration or scattered light (see §3.4). At lower altitudes this factor is also higher than possible uncertainties associated with either the density line ratio or elemental abundances alone. This occurs in both the cavity and streamer. In the cavity there is significant variation at a given altitude, but this is likely due to substructure variations that we are not modeling (see § 4.1).

A possible explanation for the low ratio of data to model in the EUV would be the presence of small scale variations in the plasma that are not described in the model. Such structures would have to be below the resolution at which we are analyzing the data. The model density is derived from a EUV line ratio. Such ratios only represent the material emitting in the lines used, in this case plasma near the peak response for Fe XII, $\log T(\mathrm{K}) \approx$ 6.25. If there is a significant amount of plasma that does not produce much emission in those lines the line ratio derived density will be significantly different from the average density. This might be the case if some of the plasma is at a much lower density or at a substantially different temperature. Filling factors describing the fraction of volume occupied by emitting

material are, in fact, derived by comparisons of line ratios and intensity-based emission measures.

Filling factors on the order of 0.1 or even smaller have been recorded in numerous coronal features. Warren et al. (2008) find filling factors of 0.1 in a study of active region loops using EIS. Tripathi et al. (2009) used Fe XII lines to derive filling factors as low as 0.02 near loop foot points, but the factor increased to unity by an altitude of about 40 Mm. Prominence filling factor estimates fall in a wide range from 0.01 to 0.2 (e.g., Mariska et al. 1979; Kucera et al. 1998; Chiuderi Drago et al. 2001). Particularly relevant to these cavity observations, Hudson et al. (1999), studying a hot prominence cavity core with the *Yohkoh*/SXT data, found that if they assumed densities of 10^8 cm^{-3} (similar to those used here) they calculated that the hot region had a filling factor significantly less than unity.

However, a simple volume filling factor is difficult to reconcile with the pB data shown in Fig. 10. In a simple filamentary model in which all material is near 1 MK (and hence observable in our EUV lines) the pB data is consistent with a filling factor in the the 0.7-1 range for data between 1.17-1.25 R$_\odot$. Although the pB data do not overlap with the EUV data in altitude, the data sets come quite close together, with the EIS cavity data in the region analyzed extending to 1.163 R$_\odot$ and the pB data having a lower limit of 1.172 R$_\odot$. There is some small indication of a increase in filling factor in the EIS data, but it is not sufficient to match the much higher filling factor value indicated by the pB data.

One solution to this problem would be that a significant portion of the mass is at a temperature outside the range measured by the EIS iron lines used in our analysis (see Fig. 3). The spectral line emission is produced only in plasma in a limited temperature range, while the pB has no temperature dependence because it is produced by light scattered off of all electrons (see Eq. 6). Because the temperature dependence of the lines overlaps significantly and the different lines show similar ratios of the data to the model line intensities, it would not be possible to have significant unmodeled material in the range of the spectral lines.

Thus most of the material would have to be outside the range $\log T(\mathrm{K}) \approx 5.8 - 6.7$. There is evidence that relatively cool material may exist in the cavity over an area larger than that usually considered to be the prominence. Vourlidas et al. (2010), observing a filament in the Lyman-α line in high resolution images, found Lyman-α absorption over a significantly larger portion of the filament channel than seen in the Hα line. Schwartz et al. (2006) modeled Lyman line emission from a filament and surrounding area and suggested that the area surrounding the filament may contain substantial cool material that is not sufficient to be observed in absorption but which may still take up significant volume, thus reducing the volume inhabited by EUV emitting material.

The data-to-model ratios are essentially the same in the cavity and streamer. This may seem strange because streamers are thought of as fairly steady structures. However, some, although not all, studies of streamers indicate that they are not in hydrostatic equilibrium (see Aschwanden & Acton 2001; Warren & Warshall 2002). If that is the case one might expect streamers to exhibit a dynamic heating, cooling, and condensation cycle as often discussed for active region loops (see, e.g., review by Klimchuk 2006) that could result in a significant amount of very hot mass (above our observation range) from the initial energy release and cool mass (mostly at chromospheric temperatures) in the form of condensations. To check the plausibility of such an idea one would want to combine of a model of dynamically heated loops (e.g., the thermal nonequilibrium model) combined with non-local thermodynamic equilibrium (non-LTE) modeling to correctly estimate likely intensities of condensations in the cooler lines, like Hα.

4.3. Prominence

The focus of this paper is the prominence cavity rather than the prominence itself. The prominence may be viewed as a tightly coupled part of the prominence cavity, but one that presents different analysis challenges because of its cool, dense plasma that results in emission in lines that can be optically thick and include radiatively scattered components and Lyman continuum absorption in the EUV. Thus a detailed analysis is beyond the scope of this paper. Still, we can make some observations about the properties of the prominence itself. The extent of the prominence in EIT 304 Å and the EIS Fe VIII are similar; it is more extensive in these lines than in the Lyman absorption seen in the Fe XII 195.1 Å line. The Fe VIII line response peaks at $\log T(\text{K}) = 5.7$ and it frequently exhibits prominence emission (e.g., Labrosse et al. 2011).

We also note that there is prominence emission in both the Fe X 184.5 Å and Fe XI 188.2 Å, lines, indicating that there is material at even hotter temperatures in the prominence-corona transition regions (PCTR). The presence of such emission should be taken into account in attempts to model the PCTR. Searching through the Chianti database, we have not found any line blends with cooler lines that are likely to be contributing to this emission. Conversely, the Fe XIV 274.1 Å and Fe XV 284.2 Å lines show a lack of emission in areas in which there is emission at lower temperatures, particularly in the area near (-730″,700″) in Fig. 1. This could be due to a lack of relatively high temperature emission, but it is also possible there is a contribution from Lyman absorption, which would be different for 274-285 Å than in the 185-195 Å range (see Heinzel et al. 2008).

Emission associated with prominences has been seen in the 171 Å bands of EUV imaging

instruments such as the *Transition Region and Coronal Explorer (TRACE)* and the *Solar Dynamics Observatory*'s Atmospheric Imaging Assembly (*SDO*/AIA) which are dominated by Fe IX, but, because the wavelength responses of these instruments are relatively wide (e.g., Lemen et al. 2011), is has not been clear if this emission is due to emission from the Fe IX or to other cooler lines in the bandpasses. Of course, the presence of actual Fe IX emission does not rule out the possibility of an additional component in the prominence 171 Å band emission observed by EUV imaging instruments.

5. Summary and Conclusions

Building on earlier forward modeling of this cavity and streamer to determine geometry and density profiles (Gibson et al. 2010; Schmit & Gibson 2011), we use temperature dependent ratios of iron lines observed with *Hinode*/EIS to constrain cavity and streamer temperature. We find that a fit to the data with an altitude-dependent temperature profile indicates that both the streamer and cavity have temperatures in the range 1.4-1.7 MK, consistent with earlier measurements of streamer temperatures. However, the data clearly show significant temperature substructure in the cavity that cannot be described with a simple function of radius. This is consistent with other observations of significant substructure in cavities evident in hot cavity sources (Hudson et al. 1999; Reeves et al. 2012) and velocity signatures (Schmit et al. 2009; Wang & Stenborg 2010). It seems likely that these structures are projections of cavity magnetic field with varying plasma conditions between and perhaps along different magnetic field lines in the cavity. Understanding such structures may be a key to determining the magnetic field structure of the cavity and thus the entire pre-CME magnetic configuration.

We find that the model overestimates the EUV line intensity by a radially decreasing factor of 10 to 4. This suggests a filling factor in the range 0.1-0.2. However, the pB data indicate that significantly more mass is present. A possible explanation is that there is a substantial amount of material present that is not in the temperature range covered by the iron lines ($\approx 0.8 - 4$ MK). This would be consistent with studies indicating there may be significant amounts of material with $T \lesssim 30,000$ K in the cavity beyond the prominence (Schwartz et al. 2006; Vourlidas et al. 2010). That the effect also appears in the streamer would be consistent with a dynamic model of streamers exhibiting heating and cool condensations.

Acknowledgements

REFERENCES

Alexander, D. 1999, J. Geophys. Res., 104, 9701

Aschwanden, M. J., & Acton, L. W. 2001, ApJ, 550, 475

Billings, D. E. 1966, A Guide to the Solar Corona (New York: Academic Press)

Chiuderi Drago, F., Alissandrakis, C. E., Bastian, T., Bocchialini, K., & Harrison, R. A. 2001, Sol. Phys., 199, 115

Culhane, J. L., et al. 2007, Sol. Phys., 243, 19

Del Zanna, G. 2010, A&A, 514, A41

Dere, K. P., Landi, E., Mason, H. E., Monsignori Fossi, B. C., & Young, P. R. 1997, A&AS, 125, 149

Dere, K. P., Landi, E., Young, P. R., Del Zanna, G., Landini, M., & Mason, H. E. 2009, A&A, 498, 915

Elmore, D. F., Burkepile, J. T., Darnell, J. A., Lecinski, A. R., & Stanger, A. L. 2003, in Society of Photo-Optical Instrumentation Engineers (SPIE) Conference Series, Vol. 4843, Society of Photo-Optical Instrumentation Engineers (SPIE) Conference Series, ed. S. Fineschi, 66

Feldman, U. 1992, Phys. Scr, 46, 202

Feldman, U., Doschek, G. A., Schühle, U., & Wilhelm, K. 1999, ApJ, 518, 500

Feldman, U., Mandelbaum, P., Seely, J. F., Doschek, G. A., & Gursky, H. 1992, ApJS, 81, 387

Feldman, U., Schühle, U., Widing, K. G., & Laming, J. M. 1998, ApJ, 505, 999

Feldman, U., Warren, H. P., Brown, C. M., & Doschek, G. A. 2009, ApJ, 695, 36

Feldman, U., & Widing, K. G. 2002, Physics of Plasmas, 9, 629

Fuller, J., & Gibson, S. E. 2009, Astrophys. Journ., 700, 1205

Fuller, J., Gibson, S. E., de Toma, G., & Fan, Y. 2008, Astrophys. Journ., 678, 515

Gibson, S. E., Fludra, A., Bagenal, F., Biesecker, D., del Zanna, G., & Bromage, B. 1999, J. Geophys. Res., 104, 9691

Gibson, S. E., Foster, D., Burkepile, J., de Toma, G., & Stanger, A. 2006, ApJ, 641, 590

Gibson, S. E., Foster, D. J., Guhathakurta, M., Holzer, T., & St. Cyr, O. C. 2003, Journal of Geophysical Research (Space Physics), 108, 1444

Gibson, S. E., et al. 2010, ApJ, 724, 1133

Guhathakurta, M., Rottman, G. J., Fisher, R. R., Orrall, F. Q., & Altrock, R. C. 1992, Astrophys. Journ., 388, 633

Habbal, S. R., Druckmueller, M., Morgan, H., Scholl, I., Rusin, V., Daw, A., Johnson, J., & Arndt, M. 2010, Astrophys. Journ., 719, 1362

Hahn, M., Landi, E., & Savin, D. W. 2011, ApJ, 736, 101

Heinzel, P., et al. 2008, ApJ, 686, 1383

Hudson, H. S., Acton, L. W., Harvey, K. L., & McKenzie, D. E. 1999, ApJ, 513, L83

Karpen, J. T., & Antiochos, S. K. 2008, Astrophys. Journ., 676, 658

Klimchuk, J. A. 2006, Sol. Phys., 234, 41

Kucera, T. A., Andretta, V., & Poland, A. I. 1998, Solar Phys., 183, 91

Labrosse, N., Schmieder, B., Heinzel, P., & Watanabe, T. 2011, A&A, 531, A69

Landi, E., Del Zanna, G., Young, P., Dere, K., & Mason, H. 2011, Astrophys. Journ., in press

Lang, J., et al. 2006, Appl. Opt., 45, 8689

Lemen, J. R., et al. 2011, Sol. Phys., 241

Luna Bennasar, M., Karpen, J., & DeVore, C. 2012, Astrophys. Journ., in press

Mariska, J. T., Doschek, G. A., & Feldman, U. 1979, ApJ, 232, 929

Nelder, J. A., & Mead, R. 1965, Computer Journal, 7, 308

Parenti, S., Bromage, B. J. I., Poletto, G., Noci, G., Raymond, J. C., & Bromage, G. E. 2000, A&A, 363, 800

Parenti, S., Landi, E., & Bromage, B. J. I. 2003, ApJ, 590, 519

Reeves, K., Gibson, S., Kucera, T., Hudson, H., & Kano, R. 2012, Astrophys. Journ., in press

Schmit, D. J., & Gibson, S. E. 2011, Astrophys. Journ., 733, 1

Schmit, D. J., Gibson, S. E., Tomczyk, S., Reeves, K. K., Sterling, A. C., Brooks, D. H., Williams, D. R., & Tripathi, D. 2009, ApJ, 700, L96

Schwartz, P., Heinzel, P., Schmieder, B., & Anzer, U. 2006, A&A, 459, 651

Spicer, D. S., Feldman, U., Widing, K. G., & Rilee, M. 1998, ApJ, 494, 450

Tripathi, D., Mason, H. E., Dwivedi, B. N., del Zanna, G., & Young, P. R. 2009, ApJ, 694, 1256

Ugarte-Urra, I. 2010, EIS Software Note 12, ver. 1.0

Vásquez, A. M., Frazin, R. A., & Kamalabadi, F. 2009, Sol. Phys., 256, 73

Vourlidas, A., Sanchez Andrade-Nuño, B., Landi, E., Patsourakos, S., Teriaca, L., Schühle, U., Korendyke, C. M., & Nestoras, I. 2010, Sol. Phys., 261, 53

Wang, Y.-M., & Stenborg, G. 2010, ApJ, 719, L181

Warren, H. P., & Brooks, D. H. 2009, ApJ, 700, 762

Warren, H. P., Ugarte-Urra, I., Doschek, G. A., Brooks, D. H., & Williams, D. R. 2008, ApJ, 686, L131

Warren, H. P., & Warshall, A. D. 2002, ApJ, 571, 999

Young, P. 2011, EIS Software Note 1, ver. 3.3

Young, P. R., Watanabe, T., Hara, H., & Mariska, J. T. 2009, A&A, 495, 587